A Process-Oriented Diagnostic to Assess Precipitation-Thermodynamic Relations and Application to CMIP6 Models

Fiaz Ahmed[1] [ID] **and J. David Neelin[1]** [ID]

[1]Atmospheric and Oceanic Sciences, University of California, Los Angeles, CA, USA

Abstract A process-oriented diagnostic (POD) is introduced to measure the thermodynamic sensitivity of convection in climate models. The physical basis for this POD is the observed tropical precipitation-buoyancy relationship. Fast timescale precipitation and thermodynamic profiles over oceans are POD inputs; these are used to evaluate model precipitation sensitivities to lower-tropospheric measures of subsaturation ($SUBSAT_L$) and undilute conditional instability. The POD is used to diagnose 24 coupled model inter-comparison project phase six (CMIP6) models. Half the diagnosed models exhibit $SUBSAT_L$ sensitivity close to observed, while six models are excessively sensitive. Parameter perturbation experiments with the Community Atmospheric Model (CAM5) support the physical basis for the POD. Increasing entrainment increases the CAM5 precipitation $SUBSAT_L$ sensitivity. Switching off the convective scheme or modifying the convective trigger to be oversensitive to moisture reproduces the excessive $SUBSAT_L$ sensitivity seen among CMIP6 models. Models with excessive $SUBSAT_L$ sensitivities have precipitating mean states closer to grid-scale saturation and likely support more grid-scale convection.

Plain Language Summary Climate models have difficulties in capturing accurate rainfall statistics. A primary reason is that they disagree on how sensitive rainfall ought to be to atmospheric moisture, when compared to near-surface warmth. For simplicity, let us call this the moisture-temperature sensitivity of rainfall. We know what this looks like from observations. We present a new method to compare the moisture-temperature sensitivity in climate models to observations. We apply this method to check how well the state-of-the-art climate models perform. We find that in about half the models, rainfall has close to the right moisture-temperature sensitivity. This is good news. In earlier generations, climate model rainfall has not been sensitive enough to moisture. However, rainfall in some models is over-sensitive to moisture. We perform experiments with a climate model to examine why. Our experiments highlight two possible reasons: (a) the clouds in these models may not act fast enough to remove excess moisture from the air or (b) the model may have been tuned to make clouds more sensitive to moisture but has overshot the mark. This experiment is presented as a proof of concept for how a model developer would use our moisture-temperature sensitivity tool to improve their model.

1. Introduction

Modern-day climate models suffer from multiple precipitation-related biases. A variety of phenomena—particularly in the tropics—are compromised by uncertainties in deep convective schemes. Examples include the time-mean precipitation structure (Chikira, 2010; Mapes & Neale, 2011; Oueslati & Bellon, 2013), the El Niño Southern Oscillation (Neale et al., 2008; Watanabe et al., 2011), the Madden Julian Oscillation (Ahn et al., 2017; Zhang & Song, 2009), the diurnal cycle of precipitation (Wang et al., 2007; Xie et al., 2019) and precipitation probability distributions (Hirota et al., 2014; Kooperman et al., 2018). Precipitation-related biases persist (S. M. Hagos et al., 2021; Tian & Dong, 2020) into the generation of climate models participating in phase six of the coupled model inter-comparison project (CMIP6; Eyring et al., 2016). Model diagnostics play a key role in the iterated improvement of climate models. In a model development work-flow, process-oriented diagnostics (PODs; Maloney et al., 2019)—that target a specific physical property of the model—are particularly valuable. This is because PODs provide actionable feedback to parameterization and model developers, with information about specific parameters or model components requiring re-calibration.

An important physical property of atmospheric models is the lower-tropospheric moisture sensitivity of convection. This property affects both model mean state and variability. For instance, increased moisture sensitivity of convection enhances model intraseasonal variability, but degrades the mean state (Hannah & Maloney, 2011, 2014; Kim et al., 2011). Several PODs target model convection's free-tropospheric moisture sensitivity (Jiang et al., 2016; Kim et al., 2014; Kuo et al., 2020; S. Hagos et al., 2019; S. M. Hagos et al., 2021; Rushley et al., 2018; Wolding et al., 2020). These PODs are motivated by the robust, observed relationship between tropical precipitation and column-integrated moisture (Ahmed & Schumacher, 2015; Bretherton et al., 2004; Holloway & Neelin, 2009; Peters & Neelin, 2006; Raymond, 2000).

The physical basis for the precipitation-moisture relationship is cloud dilution by dry tropospheric air (Holloway & Neelin, 2009; Schiro et al., 2016). The precipitation-moisture relationship can be recast as a general precipitation-buoyancy relationship (Adames et al., 2021; Ahmed & Neelin, 2018; Schiro et al., 2018). The buoyancy here is that of a convective updraft entraining environmental air. The entrainment profile is empirically informed and effectively weights lower troposphere vertical levels according to their contributions to updraft mass-flux. This buoyancy recasting exercise clarifies that the dilution effects deplete the undilute buoyancy (Ahmed & Neelin, 2021) supplied by differences between boundary layer enthalpy and free tropospheric temperature.

In this study, we introduce a POD—based on the observed precipitation-buoyancy relationship—to simultaneously assess the dependence of model convection on two effects: (a) an undilute buoyancy measuring environmental conditional instability in the absence of lower-tropospheric entrainment, and (b) buoyancy dilution by dry, lower free-tropospheric air. A reference baseline for the POD using re-analysis and satellite data is established in Section 3. In Section 4, the POD is applied to a set of CMIP6 models. The POD shows that several models have lower-tropospheric moisture sensitivity—relative to undilute buoyancy—within the baseline uncertainty range. A handful of models are either excessively or inadequately sensitive to lower-tropospheric moisture. Parameter perturbation experiments in Section 5 yield prototypes for the range of behavior noted among CMIP6 models, and elucidate the physical basis for the POD.

2. The Precipitation-Buoyancy Relationship POD

2.1. Definitions and Data

Following Ahmed et al. (2020) and Adames et al. (2021), a lower-tropospheric averaged buoyancy measure B_L is defined as:

$$B_L = \frac{g}{\overline{\kappa}_L \theta_{e0}} \left[w_B \underbrace{\left(\frac{\theta_{eB} - \theta_{eL}^*}{\theta_{eL}^*} \right) \theta_{e0}}_{\text{CAPE}_L} - w_L \underbrace{\left(\frac{\theta_{eL}^* - \theta_{eL}}{\theta_{eL}^*} \right) \theta_{e0}}_{\text{SUBSAT}_L} \right]. \tag{1}$$

In Equation 1, θ_e is the equivalent potential temperature; θ_{eB} is θ_e averaged over a nominal atmospheric boundary layer (ABL). The ABL is taken to be the lowest 100 hPa layer above surface. Terms θ_{eL} and θ_{eL}^* are the θ_e and saturated θ_e respectively averaged over the lower-free troposphere (LFT). The LFT is taken to be the layer between the top of the ABL and the 500 hPa level. In Equation 1, θ_{e0} is a reference θ_e value (=340 K), $\overline{\kappa}_L$ is a constant (=3.0; see Text S1), and g is the acceleration due to gravity (=9.8 ms^{-2}). The term CAPE$_L$ in Equation 1 is a measure of the undilute plume buoyancy—akin to convective available potential energy (CAPE) computed using grid-scale thermodynamic profiles from the lower troposphere. The term SUBSAT$_L$ measures the degree of subsaturation in the LFT. Weights w_B and w_L depend on the ratio of the ABL and LFT thicknesses (Text S1) and represent the typical fraction of air entrained into a convecting plume from each layer. While B_L has units of ms^{-2}, the scaling factor θ_{e0} is used to present CAPE$_L$ and SUBSAT$_L$ in units of K.

The POD observational baseline is constructed using 3-hourly ERA5 (Hersbach et al., 2020) temperature and specific humidity profiles. The B_L values computed using Equation 1 are spatio-temporally matched to 3-hourly precipitation values from the Tropical Rainfall Measuring Mission (TRMM 3B42; Huffman et al., 2007). Both ERA5 and TRMM output from years 2002–2014 are used only over tropical ocean points
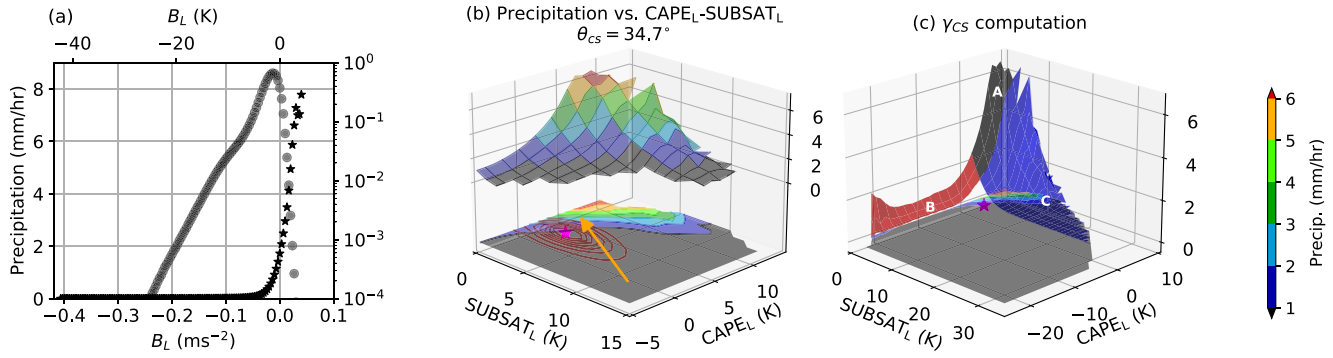
Figure 1. (a) The ERA5/TRMM 3B42 precipitation-B_L relationship (left axis) and the B_L pdf for precipitating points (right axis). The top axis shows B_L in units of K. (b) The 2D TRMM 3B42 precipitation conditionally averaged by $CAPE_L$ and $SUBSAT_L$ (colored 2D contours). The sharp increase in conditional-mean precipitation is reproduced as a 2D surface and is shifted along the z-axis for clarity. The maroon contours represent the 2D precipitating pdf; the mode of this pdf is indicated by the magenta star marker. The orange arrow is the γ_{CS} vector summarizing the precipitation gradient (see text; a magnitude of 0.25 mm hr^{-1} K^{-1} is displayed as a length of 10 K in the $CAPE_L$-$SUBSAT_L$ plane). The z-axis has units of mm/hr; the colors in the precipitation surface have the same units with values shown in the colorbar. (c) Steps involved in γ_{CS} computation. Note differences in x- and y-axis ranges between (b and c).

from 20°N–20°S. High (0.25° × 0.25°) and low (2.0° × 2.0°) horizontal resolution versions of the ERA5/TRMM 3B42 datasets are used to quantify sensitivities to resolution and to establish the baseline uncertainty range.

2.2. Observational Baseline

Figure 1 sets the observational baseline for the precipitation-B_L relationship using the high-resolution ERA5/TRMM 3B42 data. The precipitation conditionally averaged by B_L is shown in Figure 1a. There exists little-to-no conditional-mean precipitation below a threshold B_L value, but strong precipitation above it. The precipitating probability density function (pdf) of B_L—for points precipitating above 0.25 mm/hr—peaks just below the threshold B_L value for strong precipitation. This indicates a balance between the slow times-cale generation of B_L and its fast timescale consumption by convection and associated precipitation. The upper x-axis in Figure 1a shows B_L scaled by $(\bar{\kappa}_L \theta_{e0})/g$ to have the same units (K) as $CAPE_L$ and $SUBSAT_L$. Figure 1b shows a two-dimensional (2D) 'precipitation surface', which is the TRMM 3B42 precipitation conditionally averaged by $CAPE_L$ and $SUBSAT_L$. As seen from Equation 1, a scaled and weighted difference between $CAPE_L$ and $SUBSAT_L$ yields B_L. Increments in $CAPE_L$ (more undilute buoyancy) and decrements in $SUBSAT_L$ (closer to LFT saturation) both produce strong precipitation increases. A 2D precipitation on-set occurs for transitions between low $CAPE_L$/high $SUBSAT_L$ (stable/dry) and high $CAPE_L$/low $SUBSAT_L$ (unstable/moist) environments. Although the information in Figure 1b can be presented with a 2D contour plot (Figure S1), the three-dimensional perspective provides additional visual emphasis on the precipitation pickup.

The joint precipitating pdf (>0.25 mm/hr) of $CAPE_L$ and $SUBSAT_L$ is also shown in Figure 1b. Note that results here are insensitive to the actual value of the precipitating threshold. As for the marginal precipitat-ing B_L pdf in Figure 1a, the mode of this joint pdf is situated on the edge of the 2D precipitation onset. This property allows the construction of a metric γ_{CS} to assess the relative sensitivity of TRMM 3B42 precipita-tion to variations in $CAPE_L$ versus $SUBSAT_L$. The construction of this metric is elaborated in Figure 1c. The location of the precipitating pdf mode is used to divide the precipitation surface into three nonoverlapping regions: A, B and C. Precipitation increases for transitions from regions B to A—with a nearly invariant $SUBSAT_L$—provide a measure of the $CAPE_L$ sensitivity of precipitation. A similar precipitation increase between regions C and A provides a measure of the $SUBSAT_L$ sensitivity. A vector is now defined as a fi-nite-difference gradient of precipitation in the $CAPE_L$-$SUBSAT_L$ plane with magnitude:

$$|\gamma_{CS}| = \sqrt{\left(\frac{P_A - P_B}{CAPE_{LA} - CAPE_{LB}}\right)^2 + \left(\frac{P_A - P_C}{SUBSAT_{LA} - SUBSAT_{LC}}\right)^2}, \quad (2)$$

where P_A, $CAPE_{LA}$ and $SUBSAT_{LA}$ are the precipitation, $CAPE_L$ and $SUBSAT_L$ respectively averaged over region A in Figure 1c. A similar notation holds for quantities with subscripts B and C in Equation 2. The magnitude of γ_{CS} in Equation 2 measures the strength of the precipitation onset or the 'pickup'. The angle between γ_{CS} and the $SUBSAT_L$ axis in Figure 1b is termed θ_{CS} and defined:

$$\tan\theta_{CS} = \frac{P_A - P_B}{CAPE_{LA} - CAPE_{LB}} \times \frac{SUBSAT_{LA} - SUBSAT_{LC}}{P_A - P_C}. \tag{3}$$

The angle θ_{CS} gives the direction of the gradient of the precipitation surface. The ratio $\tan\theta_{CS}$ is between partial derivatives estimated from point A along the $CAPE_L$ and $SUBSAT_L$ directions. It thus summarizes the *relative* precipitation sensitivities to $CAPE_L$ and $SUBSAT_L$. In Figure 1 and in subsequent similar figures, the head of the vector γ_{CS} is positioned on a point in the $CAPE_L$-$SUBSAT_L$ plane with co-ordinates: ($CAPE_{LA}$, $SUBSAT_{LA}$).

If $\theta_{CS} = 90°$, γ_{CS} is parallel to the $CAPE_L$ axis, and the precipitation is solely sensitive to $CAPE_L$ perturbations. This represents a case with negligible entrainment in the LFT in which the undilute B_L entirely governs precipitation. If precipitation is equally sensitive to $CAPE_L$ and $SUBSAT_L$ perturbations, then $\theta_{CS} = 45°$. When $\theta_{CS} = 0°$, precipitation is only sensitive to $SUBSAT_L$ perturbations, without influence from undilute buoyancy. The ERA5/TRMM 3B42 precipitation surface has $\theta_{CS} \sim 34.7°$, suggesting greater relative $SUBSAT_L$ sensitivity, likely due to the ledge-like region B in Figure 1b. Within this region, the conditional-mean precipitation is nearly invariant over a large range of $CAPE_L$ values (~ -20–0 K).

Similar statistics as in Figure 1 are also noted for the low-resolution observational baseline (Text S3 and Figure S2). The measures $|\gamma_{CS}|$ and θ_{CS} condense information about the thermodynamic sensitivity of tropical convection into a form that allows estimation and comparison across datasets, and has a simple visual representation. This property forms the basis for the precipitation-buoyancy relationship POD, which is applied to a set of CMIP6 models in the following section.

3. Application to CMIP6 Models

Twenty-four models from the CMIP6 archive were analyzed. The POD targets fast timescale processes, so sub-daily samples over a two-year time period are sufficient to construct the precipitation-buoyancy statistics. For most models, 3-hourly averaged precipitation, and 6-hourly instantaneous temperature and specific humidity fields from the historical runs are used. Outliers from this general case, along with details about model horizontal resolutions and time periods analyzed are in Text S4 and Table S1. As for the observational baseline, only tropical ocean points between 20°N–20°S are used. Figure 2a presents precipitation conditionally averaged by B_L for the CMIP6 models. Figure 2b presents the parameters of the γ_{CS} vector—$|\gamma_{CS}|$ and θ_{CS}—on a polar plot. A bootstrapping procedure is used to generate an uncertainty measure for the observational baseline; this accounts for differences in the analysis periods between observations (13 years) and models (2 years). More information on the bootstrapping procedure is given in Text S2. Both the high- and low-resolution versions of the observational baseline—which bracket the different CMIP6 model resolutions—are shown in Figure 2.

Several CMIP6 models capture the sharp precipitation-B_L relationship (Figure 2a). A few model precipitation fields (CNRM-CM6-1-HR, MRI-ESM2-0, FGOALS-g3, MIROC6) show high sensitivity to B_L—as measured by conditional-mean precipitation larger than 6 mm/hr. A few models have weak precipitation-B_L relationships with conditional-mean precipitation <2 mm/hr; these include the IPSL models, the MPI models, AWI-ESM1 and MIROC-ES2L. Model horizontal resolution is not a universal indicator of the precipitation-B_L relationship strength. This is consistent with the fact that the low-resolution ERA5/TRMM 3B42 data set has $|\gamma_{CS}|$ and θ_{CS} values comparable to the high-resolution version (Figure 2b). However, for the same model, the high-resolution version shows greater pickup strength than the low-resolution version; this is best exemplified by comparing CNRM-CM6-1 with CNRM-CM6-1-HR. Each model precipitation field responds to an internal buoyancy measure that varies between convective schemes and does not necessarily correspond to B_L. Despite this, most model precipitation
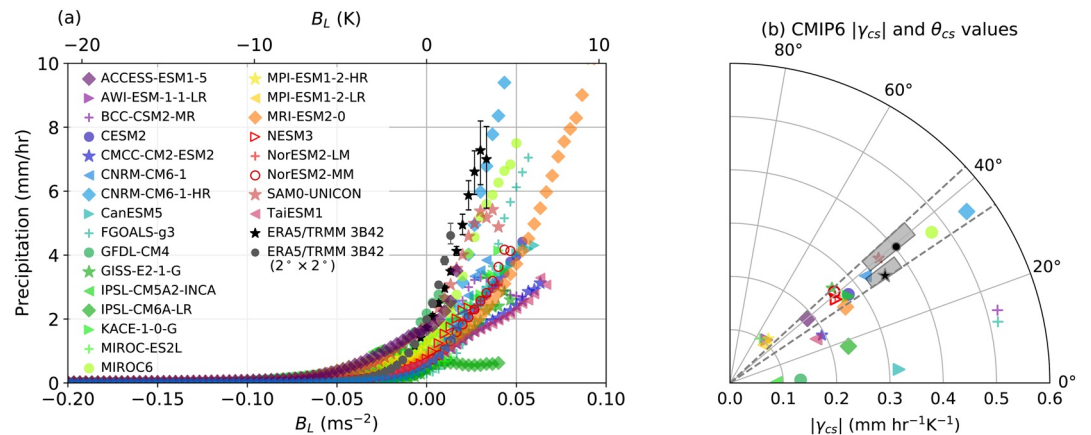
Figure 2. (a) The precipitation-B_L relationship for 24 analyzed CMIP6 models. The ERA5/TRMM 3B42 curves (0.25° version in black stars; 2.0° version in gray circles) form the observational baseline. (b) Parameters of the γ_{CS} vector for each model represented in a polar plot. The ERA5/TRMM 3B42 γ_{CS} values are represented by the black star (0.25° version) and black circle (2.0° version) markers. A bootstrapping procedure is used to estimate the observational uncertainty (Text S2). The error bars around the black star and gray solid markers in (a) denote the 5th–95th percentile in conditional-mean precipitation. The shaded regions around the observational baseline markers in (b) bound the 5th–95th percentile of $|\gamma_{CS}|$ and θ_{CS} values. The dashed gray lines in (b) bound θ_{CS} values in the observational baseline between the 5th percentile of the 0.25° version and the 95th percentile of 2.0° version.

fields exhibit sensitivity to B_L. This is presumably due to qualitatively similar underlying physics in parameterization assumptions.

Figure 2b displays the model precipitation CAPE$_L$-SUBSAT$_L$ sensitivity on a polar plot. The location of each model on this plot has co-ordinates ($|\gamma_{CS}|$, θ_{CS}). Half the analyzed models (12 out of 24) have CAPE$_L$-SUBSAT$_L$ sensitivities bound by uncertainties in the observational baseline ($33° \lesssim \theta_{CS} \lesssim 42°$). Examples include the CNRM-CM6 models, MIROC6, SAM0-UNICON, CESM2, MRI-ESM2-0 and GISS-E2-1-G. Four models (AWI-ESM-1-1-LR, MIROC-ES2L, and the two MPI models) have precipitation inadequately sensitive to SUBSAT$_L$ variations ($\theta_{CS} > 45°$). These models also exhibit weaker precipitation-B_L relationships (Figure 2a) and have smaller pickup strengths ($|\gamma_{CS}| \sim 0.1$ mm/hr K^{-1} in Figure 2b). Six models have $\theta_{CS} < 15°$: FGOALS-g3, BCC-CSM2-MR, GFDL-CM4, CanESM5 and the two IPSL models. These models are classified as being excessively sensitive to SUBSAT$_L$ variations. Possible reasons for this behavior are explored in the next section. In all but one pair of models (MIROC6 and MIROC-ES2L), resolution changes do not greatly impact the CAPE$_L$-SUBSAT$_L$ sensitivity.

Figure 3 shows 2D precipitation surfaces for a few select models (see Figure S3 for contour plot versions). The models (top row in Figure 3) with reasonable CAPE$_L$-SUBSAT$_L$ sensitivity and a strong precipitation pickup (CNRM-CM6-1-HR, MIROC6 and SAM0-UNICON) compare favorably with the ERA5/TRMM 3B42 precipitation surface. The strong pickup in these models is visible from the sharp increase in the precipitation surface along the z-axis. The correspondence to the observed CAPE$_L$-SUBSAT$_L$ sensitivity can also be seen by comparing their γ_{CS} vectors in Figure 3 to that of the observational baseline. Models CESM2 and NorESM2-MM have smaller $|\gamma_{CS}|$ values, but similar θ_{CS} values to observed. As in Figure 1b, the mode of the precipitating pdfs in these models is close to the precipitation onset.

The bottom row in Figure 3 shows precipitation surfaces for models with over-sensitivity to SUBSAT$_L$. These models have small θ_{CS} values—also seen in the differences between their γ_{CS} vectors and that of ERA5/TRMM 3B42. Among these models, FGOALS-g3, BCC-CSM2-MR and CanESM5 have relatively strong pickups (also inferred from their $|\gamma_{CS}|$ values in Figure 2b). Both GFDL-CM4 and IPSL-CM6A-LR have weak precipitation pickup strengths, but their strong SUBSAT$_L$ sensitivity can be deduced by following the precipitation contours on the CAPE$_L$-SUBSAT$_L$ plane in Figure 3. The precipitating pdfs for FGOALS-g3, BCC-CSM2-MR, CanESM5 and IPSL-CM6A-LR illustrate a consequence of excessive SUBSAT$_L$ sensitivity for model mean states. When compared with the observational baseline, these four
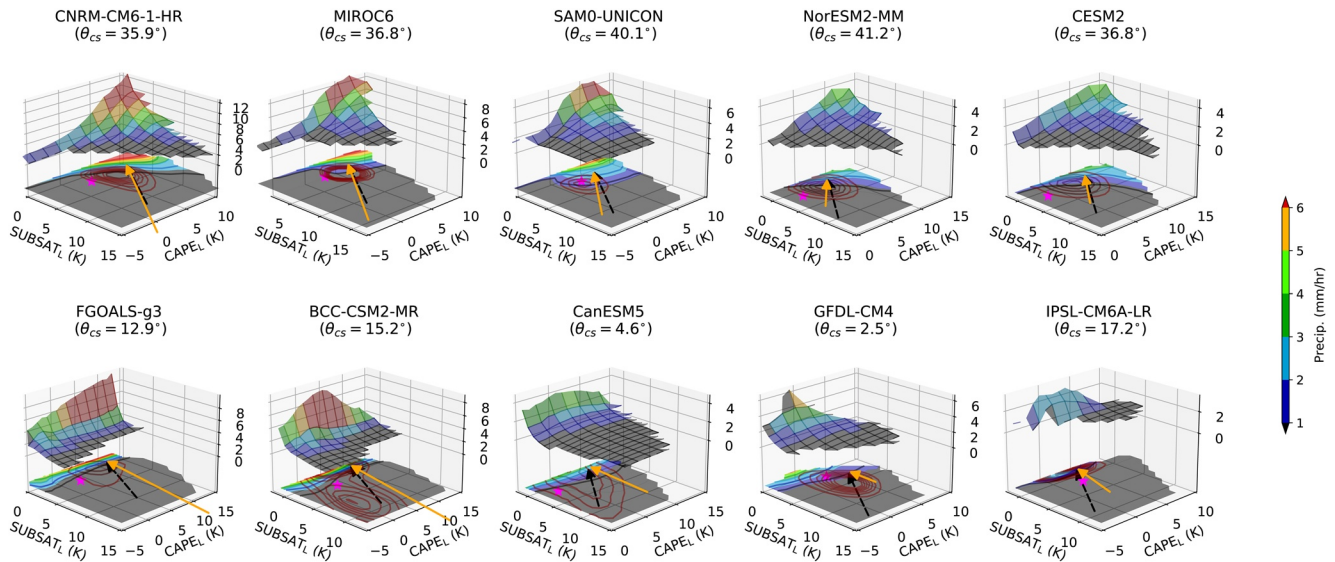
Figure 3. As in Figure 2b but for select phase six of the CMIP6 models. Note the one difference from Figure 2b: the magenta star in each panel denotes the mode of the 0.25° ERA5/TRMM 3B42 precipitating pdf. The model precipitating pdfs are denoted by maroon contours. The top row depicts models with θ_{CS} values close to observed. The bottom row depicts models with excessive SUBSAT$_L$ sensitivity ($\theta_{CS} \lesssim 15°$). Also note the varying z-axis range between each panel.

models have their precipitating pdf modes closer to LFT saturation (SUBSAT$_L \sim 0$). These models therefore saturate their lower troposphere to generate sizeable precipitation—an indicator of "gridpoint" storms (I. M. Held et al., 2007).

4. Parameter Perturbation Experiments With CAM5

We now turn to parameter perturbation experiments with version 5 of the Community Atmospheric Model (CAM5; Neale et al., 2012). These experiments serve two purposes: (a) they verify that the γ_{CS} metric indeed captures the CAPE$_L$-SUBSAT$_L$ sensitivity of model convection and (b) they generate prototypes for the observed diversity among CMIP6 models. The CAM5 model was run at a 0.9° × 1.25° horizontal resolution with fixed sea surface temperatures. The CAM5 convective parameterization is the Zhang-McFarlane (ZM) scheme (Zhang & McFarlane, 1995). The entrainment parameter within the ZM scheme closure (Neale et al., 2008) is perturbed with a series of multipliers ranging from 0.125 to 1.25 times the control value. To demonstrate the impact of other parametric changes, two additional experiments are carried out: RHTRIG and ZMOFF. In RHTRIG, the trigger function in the ZM scheme is modified; deep convection only occurs when the column relative humidity (CRH) exceeds 0.95 and when the entraining CAPE exceeds 100 J/kg. In ZMOFF, the convective scheme is turned off, so any convective motion must occur within the resolved physics. An initial 1-year spin-up run is used to branch off the various perturbation runs. Each perturbation run extends to a 2-year time period. Precipitation, and vertical profiles of temperature and specific humidity were output every 3 h.

Figure 4a–4g illustrate the changes to the CAM5 precipitation surface in response to parameter perturbations in the ZM scheme. For small entrainment (Figure 4a), the precipitation surface is oriented more toward the CAPE$_L$ direction, as also inferred from the large θ_{CS} value. The precipitating pdf is situated on the edge of the precipitation onset as expected, but the mode of the precipitating pdf occurs in a drier state when compared to ERA5/TRMM 3B42; the pickup also begins at lower values of CAPE$_L$. As the entrainment increases toward the control value (Figure 4b–4e), the θ_{CS} value decreases to become nearly parallel with the observational baseline γ_{CS} vector (Figure 4d). This change is consistent with the expectation that increased entrainment generates a stronger precipitation-moisture relationship (Kuo et al., 2017; Sahany et al., 2012). The precipitating pdf mode also shifts closer to the ERA5/TRMM 3B42 value with increasing entrainment. When the trigger function in the ZM scheme is modified to be explicitly sensitive to CRH, the precipitation is much more sensitive to SUBSAT$_L$ ($\theta_{CS} = 16.1°$ in Figure 4f). When the convective scheme
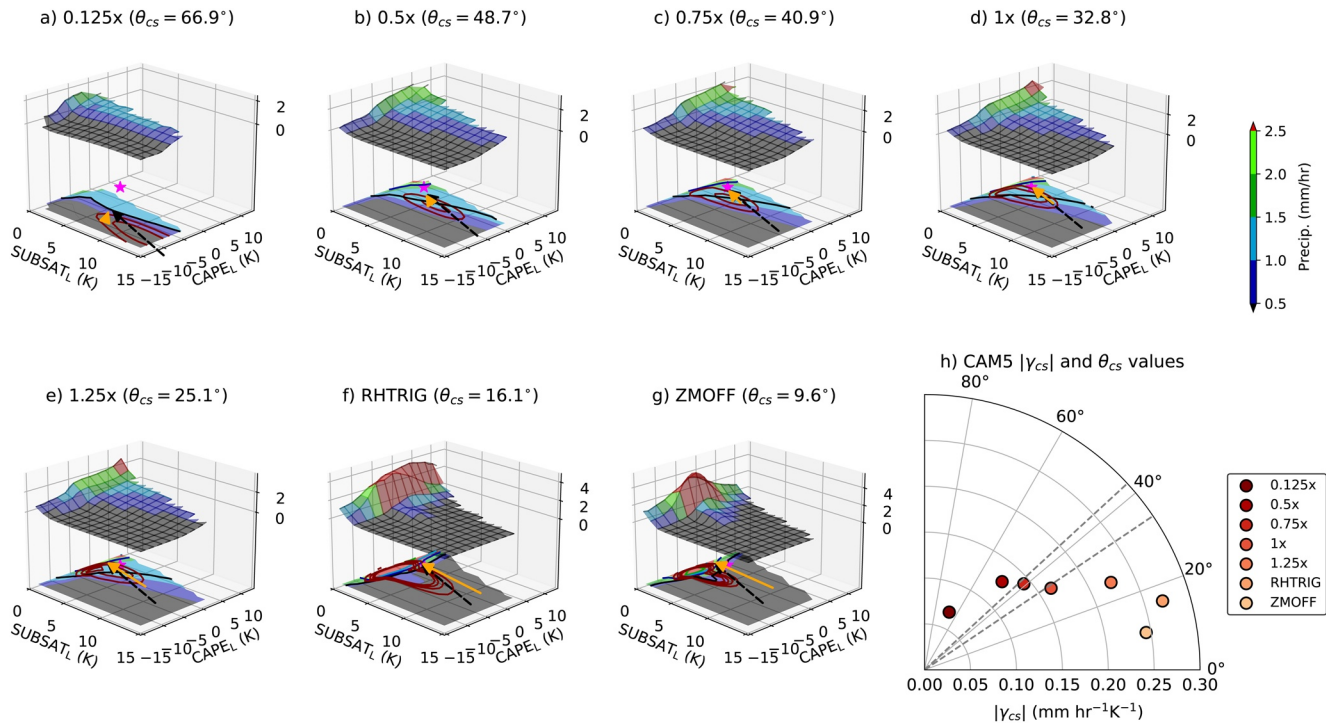
Figure 4. Panels (a–g) are the same as in Figure 1b but for Community Atmospheric Model (CAM5) parameter perturbation experiments: (a–e) are entrainment perturbations relative to control in (d); (f) perturbed trigger function and (g) ZM convective scheme off. The magenta star denotes the mode of the 0.25° ERA5/TRMM 3B24 precipitating pdf. The CAM5 precipitating pdf is denoted by maroon contours. The dashed black arrow in these panels is the ERA5/TRMM 3B42 γ_{CS} vector. Panel (h) is as in Figure 2b but for CAM5 parameter perturbation experiments (note different radial axis range). The dashed gray lines in (h) give the observed θ_{CS} range from Figure 2b.

is turned off, the CAM5 precipitation surface is almost solely sensitive to $SUBSAT_L$ ($\theta_{CS} = 9.6°$ in Figure 4g). The precipitating pdfs suggest that for the large entrainment (≥0.75x) runs, and for the RHTRIG and ZMOFF experiments (Figure 4d–4g), there is an increasing tendency for CAM5 to saturate the LFT in order to generate strong precipitation.

As entrainment increases, the model transitions from exhibiting a weak pickup, small $SUBSAT_L$ sensitivity to strong pickup and increased $SUBSAT_L$ sensitivity. As inferred from the 2D precipitation surface plots, the ZMOFF case has the greatest $SUBSAT_L$ sensitivity, while RHTRIG has large $SUBSAT_L$ sensitivity and the greatest pickup strength. Figure 4h condenses this information from Figure 4a–4g in a polar plot, similar to Figure 2b. This figure shows that (a) the γ_{CS} metric captures information about model precipitation thermodynamic sensitivity, and (b) the polar representation of this metric offers a succinct comparison across different model runs. The set of CAM5 experiments shown in Figure 4 also demonstrate a use case for the precipitation-buoyancy POD deployed during a model development/parameter tuning cycle (Hourdin et al., 2017; Mauritsen et al., 2012).

The perturbation runs from Figure 4 are also archetypes for the range of behavior noted in the CMIP6 ensemble. The low-entraining case (0.125x) with a weak pickup and small $SUBSAT_L$ sensitivity has γ_{CS} values closer to that seen for AWI-ESM-1, MIROC-ES2L and the MPI models. The adequate entrainment cases (0.75x–1x) have θ_{CS} values closer to the cluster of models with reasonable $CAPE_L$-$SUBSAT_L$ sensitivities (for example, MIROC6, SAM0-UNICON, CESM2 and the CNRM-CM6 models.). Both RHTRIG and ZMOFF experiments mimic the excessive $CAPE_L$-$SUBSAT_L$ sensitivity seen for six models in Figure 2b. An important difference, however, separates the RHTRIG and ZMOFF cases. In ZMOFF, the excessive $SUBSAT_L$ sensitivity is due to grid-scale saturation inducing large-scale rain. Whereas in RHTRIG, the parameterized convection has high sensitivity to $SUBSAT_L$ built in as a tuning assumption (Figure S5). Further analysis involving the convective rain component (Figure S4 and Text S5) suggests that RHTRIG is a prototype for

the behavior of BCC-CSM2-MR, FGOALS-g3 and the IPSL models, and ZMOFF is a prototype for the GF-DL-CM4 and CanESM5 models.

5. Conclusions

The POD introduced in this study permits quantitative assessment of the thermodynamic sensitivities of convection among CMIP6 models. Half the analyzed models have precipitation sensitivity to measures of undilute buoyancy ($CAPE_L$) and lower free tropospheric subsaturation ($SUBSAT_L$) reasonably close to observed. A handful of models have excessive precipitation sensitivity to $SUBSAT_L$. These models also have precipitating states typically closer to grid-scale saturation, pointing to the presence of frequent convection at the grid scale. Frequent grid-scale saturation can impact global radiative budgets (I. M. Held et al., 2007) and skew model precipitation probability distributions toward stronger extremes (Chan et al., 2014; Norris et al., 2021; Pendergrass & Hartmann, 2014). On the other hand, models with inadequate $SUBSAT_L$ sensitivity have weaker precipitation extremes (not shown). The POD thus offers insights into climate-system processes when the models are viewed as alternate realizations of convective physics. In CAM5, over-sensitivity to $SUBSAT_L$ is seen when the convective scheme is either switched off or when the convective trigger is made sensitive to column relative humidity. Inadequate $SUBSAT_L$ sensitivity emerges from weaker entrainment in the CAM5 convective scheme. The CAM5 parameter perturbation experiments highlight plausible parameteric choices and process-level reasons for why $CAPE_L$-$SUBSAT_L$ sensitivities among CMIP6 models depart from the observational baseline. The perturbation experiments also demonstrate a use case for how the POD would be deployed in a model development/tuning workflow.

Data Availability Statement

The ERA5 data is available at https://doi.org/10.24381/cds.bd0915c6. The TRMM 3B42 data is available from https://doi.org/10.5067/TRMM/TMPA/3H/7. The CMIP6 model data was obtained from https://esgf-node.llnl.gov/projects/esgf-llnl/. The scripts used to generate the POD metrics and plots are available at https://doi.org/10.5281/zenodo.4969120 as a part of NOAA Model Diagnostics Framework effort (https://www.gfdl.noaa.gov/mdtf-diagnostics/). Information on the various CMIP6 models can be found in the following references (see Table S1 and S2 for the corresponding models): Boucher et al. (2020); Cao et al. (2021); Cherchi et al. (2019); Danabasoglu et al. (2020); Dufresne et al. (2013); Hajima et al. (2020); I. Held et al. (2019); Kelley et al. (2020); Lee et al. (2020); Li et al. (2020); Mauritsen et al. (2019); Müller et al. (2018); Park et al. (2019); Seland et al. (2020); Semmler et al. (2020); Swart et al. (2019); Tatebe et al. (2019); Voldoire et al. (2019); Wu et al. (2019); Yukimoto et al. (2019); Ziehn et al. (2020).

References

Adames, A. F., Powell, S. W., Ahmed, F., Mayta, V. C., & Neelin, J. D. (2021). Tropical precipitation evolution in a buoyancy-budget framework. *Journal of the Atmospheric Sciences*, 78(2), 509–528. https://doi.org/10.1175/JAS-D-20-0074.1

Ahmed, F., Adames, Á. F., & Neelin, J. D. (2020). Deep convective adjustment of temperature and moisture. *Journal of the Atmospheric Sciences*, 77(6), 2163–2186. https://doi.org/10.1175/jas-d-19-0227.1

Ahmed, F., & Neelin, J. D. (2018). Reverse engineering the tropical precipitation–buoyancy relationship. *Journal of the Atmospheric Sciences*, 75(5), 1587–1608. https://doi.org/10.1175/JAS-D-17-0333.1

Ahmed, F., & Neelin, J. D. (2021). Protected convection as a metric of dry air influence on precipitation. *Journal of Climate*, 1–59.

Ahmed, F., & Schumacher, C. (2015). Convective and stratiform components of the precipitation-moisture relationship. *Geophysical Research Letters*, 42, 10–453. https://doi.org/10.1002/2015gl066957

Ahn, M.-S., Kim, D., Sperber, K. R., Kang, I.-S., Maloney, E., Waliser, D., & Hendon, H. (2017). MJO simulation in CMIP5 climate models: MJO skill metrics and process-oriented diagnosis. *Climate Dynamics*, 49(11), 4023–4045. https://doi.org/10.1007/s00382-017-3558-4

Boucher, O., Servonnat, J., Albright, A. L., Aumont, O., Balkanski, Y., Bastrikov, V., et al. (2020). Presentation and evaluation of the IPSL-CM6A-LR climate model. *Journal of Advances in Modeling Earth Systems*, 12(7), e2019MS002010.

Bretherton, C. S., Peters, M. E., & Back, L. E. (2004). Relationships between water vapor path and precipitation over the tropical oceans. *Journal of Climate*, 17(7), 1517–1528. https://doi.org/10.1175/1520-0442(2004)017<1517:rbwvpa>2.0.co;2

Cao, J., Ma, L., Liu, F., Chai, J., Zhao, H., He, Q., et al. (2021). NUIST ESM v3 data submission to CMIP6. *Advances in Atmospheric Sciences*, 38(2), 268–284. https://doi.org/10.1007/s00376-020-0173-9

Chan, S. C., Kendon, E. J., Fowler, H. J., Blenkinsop, S., Roberts, N. M., & Ferro, C. A. (2014). The value of high-resolution met office regional climate models in the simulation of multihourly precipitation extremes. *Journal of Climate*, 27(16), 6155–6174. https://doi.org/10.1175/jcli-d-13-00723.1

Cherchi, A., Fogli, P. G., Lovato, T., Peano, D., Iovino, D., Gualdi, S., et al. (2019). Global mean climate and main patterns of variability in the CMCC-CM2 coupled model. *Journal of Advances in Modeling Earth Systems*, *11*(1), 185–209.

Chikira, M. (2010). A cumulus parameterization with state-dependent entrainment rate. Part ii: Impact on climatology in a general circulation model. *Journal of the Atmospheric Sciences*, *67*(7), 2194–2211. https://doi.org/10.1175/2010jas3317.1

Danabasoglu, G., Lamarque, J.-F., Bacmeister, J., Bailey, D., DuVivier, A., Edwards, J., et al. (2020). The community earth system model version 2 (CESM2). *Journal of Advances in Modeling Earth Systems*, *12*(2). https://doi.org/10.1029/2019ms001916

Dufresne, J.-L., Foujols, M.-A., Denvil, S., Caubel, A., Marti, O., & Aumont, O. (2013). Climate change projections using the IPSL-CM5 Earth System Model: From CMIP3 to CMIP5. *Climate Dynamics*, *40*(9), 2123–2165. https://doi.org/10.1007/s00382-012-1636-1

Eyring, V., Bony, S., Meehl, G. A., Senior, C. A., Stevens, B., Stouffer, R. J., & Taylor, K. E. (2016). Overview of the coupled model intercomparison project phase 6 (CMIP6) experimental design and organization. *Geoscientific Model Development*, *9*(5), 1937–1958. https://doi.org/10.5194/gmd-9-1937-2016

Hagos, S., Leung, L. R., Ashfaq, M., & Balaguru, K. (2019). South Asian monsoon precipitation in CMIP5: A link between inter-model spread and the representations of tropical convection. *Climate Dynamics*, *52*(1), 1049–1061. https://doi.org/10.1007/s00382-018-4177-4

Hagos, S. M., Leung, L. R., Garuba, O. A., Demott, C., Harrop, B., Lu, J., & Ahn, M.-S. (2021). The relationship between precipitation and precipitable water in CMIP6 simulations and implications for tropical climatology and change. *Journal of Climate*, *34*(5), 1587–1600. https://doi.org/10.1175/JCLI-D-20-0211.1

Hajima, T., Watanabe, M., Yamamoto, A., Tatebe, H., Noguchi, M. A., Abe, M., et al. (2020). Development of the MIROC-ES2L earth system model and the evaluation of biogeochemical processes and feedbacks. *Geoscientific Model Development*, *13*(5), 2197–2244. https://doi.org/10.5194/gmd-13-2197-2020

Hannah, W. M., & Maloney, E. D. (2011). The role of moisture–convection feedbacks in simulating the Madden–Julian oscillation. *Journal of Climate*, *24*(11), 2754–2770. https://doi.org/10.1175/2011jcli3803.1

Hannah, W. M., & Maloney, E. D. (2014). The moist static energy budget in NCAR CAM5 hindcasts during DYNAMO. *Journal of Advances in Modeling Earth Systems*, *6*(2), 420–440. https://doi.org/10.1002/2013ms000272

Held, I., Guo, H., Adcroft, A., Dunne, J., Horowitz, L., Krasting, J., et al. (2019). Structure and performance of GFDL's CM4.0 climate model. *Journal of Advances in Modeling Earth Systems*, *11*(11), 3691–3727. https://doi.org/10.1029/2019ms001829

Held, I. M., Zhao, M., & Wyman, B. (2007). Dynamic radiative–convective equilibria using gcm column physics. *Journal of the Atmospheric Sciences*, *64*(1), 228–238. https://doi.org/10.1175/jas3825.11

Hersbach, H., Bell, B., Berrisford, P., Hirahara, S., Horányi, A., Muñoz-Sabater, J., et al. (2020). The era5 global reanalysis. *Quarterly Journal of the Royal Meteorological Society*, *146*(730), 1999–2049. https://doi.org/10.1002/qj.3803

Hirota, N., Takayabu, Y. N., Watanabe, M., Kimoto, M., & Chikira, M. (2014). Role of convective entrainment in spatial distributions of and temporal variations in precipitation over tropical oceans. *Journal of Climate*, *27*(23), 8707–8723. https://doi.org/10.1175/jcli-d-13-00701.1

Holloway, C. E., & Neelin, J. D. (2009). Moisture vertical structure, column water vapor, and tropical deep convection. *Journal of the Atmospheric Sciences*, *66*(6), 1665–1683. https://doi.org/10.1175/2008jas2806.1

Hourdin, F., Mauritsen, T., Gettelman, A., Golaz, J.-C., Balaji, V., Duan, Q., et al. (2017). The art and science of climate model tuning. *Bulletin of the American Meteorological Society*, *98*(3), 589–602. https://doi.org/10.1175/bams-d-15-00135.1

Huffman, G. J., Bolvin, D. T., Nelkin, E. J., Wolff, D. B., Adler, R. F., Gu, G., & Stocker, E. F. (2007). The trmm multisatellite precipitation analysis (tmpa): Quasi-global, multiyear, combined-sensor precipitation estimates at fine scales. *Journal of Hydrometeorology*, *8*(1), 38–55. https://doi.org/10.1175/JHM560.1

Jiang, X., Zhao, M., Maloney, E. D., & Waliser, D. E. (2016). Convective moisture adjustment time scale as a key factor in regulating model amplitude of the Madden-Julian oscillation. *Geophysical Research Letters*, *43*, 10–412. https://doi.org/10.1002/2016gl070898

Kelley, M., Schmidt, G. A., Nazarenko, L. S., Bauer, S. E., Ruedy, R., Russell, G. L. et al. (2020). GISS-E2.1: Configurations and climatology. *Journal of Advances in Modeling Earth Systems*, *12*(8), e2019MS002025.

Kim, D., Sobel, A. H., Maloney, E. D., Frierson, D. M., & Kang, I.-S. (2011). A systematic relationship between intraseasonal variability and mean state bias in agcm simulations. *Journal of Climate*, *24*(21), 5506–5520. https://doi.org/10.1175/2011jcli4177.1

Kim, D., Xavier, P., Maloney, E., Wheeler, M., Waliser, D., Sperber, K., et al. (2014). Process-oriented MJO simulation diagnostic: Moisture sensitivity of simulated convection. *Journal of Climate*, *27*(14), 5379–5395. https://doi.org/10.1175/jcli-d-13-00497.1

Kooperman, G. J., Pritchard, M. S., O'Brien, T. A., & Timmermans, B. W. (2018). Rainfall from resolved rather than parameterized processes better represents the present-day and climate change response of moderate rates in the community atmosphere model. *Journal of Advances in Modeling Earth Systems*, *10*(4), 971–988. https://doi.org/10.1002/2017ms001188

Kuo, Y.-H., Neelin, J. D., Chen, C.-C., Chen, W.-T., Donner, L. J., Gettelman, A., et al. (2020). Convective transition statistics over tropical oceans for climate model diagnostics: Gcm evaluation. *Journal of the Atmospheric Sciences*, *77*(1), 379–403. https://doi.org/10.1175/jas-d-19-0132.1

Kuo, Y.-H., Neelin, J. D., & Mechoso, C. R. (2017). Tropical convective transition statistics and causality in the water vapor–precipitation relation. *Journal of the Atmospheric Sciences*, *74*(3), 915–931. https://doi.org/10.1175/jas-d-16-0182.1

Lee, W.-L., Wang, Y.-C., Shiu, C.-J., Tsai, I.-C., Tu, C.-Y., Lan, Y.-Y., et al. (2020). Taiwan earth system model version 1: Description and evaluation of mean state. *Geoscientific Model Development*, *13*(9), 3887–3904. https://doi.org/10.5194/gmd-13-3887-2020

Li, L., Yu, Y., Tang, Y., Lin, P., Xie, J., Song, M., et al. (2020). The flexible global ocean-atmosphere-land system model grid-point version 3 (fgoals-g3): Description and evaluation. *Journal of Advances in Modeling Earth Systems*, *12*(9), e2019MS002012. https://doi.org/10.1029/2019ms002012

Maloney, E. D., Gettelman, A., Ming, Y., Neelin, J. D., Barrie, D., Mariotti, A., et al. (2019). Process-oriented evaluation of climate and weather forecasting models. *Bulletin of the American Meteorological Society*, *100*(9), 1665–1686. https://doi.org/10.1175/bams-d-18-0042.1

Mapes, B., & Neale, R. (2011). Parameterizing convective organization to escape the entrainment dilemma. *Journal of Advances in Modeling Earth Systems*, *3*(2). https://doi.org/10.1029/2011ms000042

Mauritsen, T., Bader, J., Becker, T., Behrens, J., Bittner, M., Brokopf, R., et al. (2019). Developments in the mpi-m earth system model version 1.2 (MPI-ESM1. 2) and its response to increasing co2. *Journal of Advances in Modeling Earth Systems*, *11*(4), 998–1038.

Mauritsen, T., Stevens, B., Roeckner, E., Crueger, T., Esch, M., Giorgetta, M., et al. (2012). Tuning the climate of a global model. *Journal of Advances in Modeling Earth Systems*, *4*(3). https://doi.org/10.1029/2012ms000154

Müller, W. A., Jungclaus, J. H., Mauritsen, T., Baehr, J., Bittner, M., Budich, R., et al. (2018). A higher-resolution version of the max planck institute earth system model (MPI-ESM1. 2-HR). *Journal of Advances in Modeling Earth Systems*, *10*(7), 1383–1413. https://doi.org/10.1029/2017ms001217

Neale, R. B., Chen, C.-C., Gettelman, A., Lauritzen, P. H., Park, S., Williamson, D. L., et al. (2012). *Description of the ncar community atmosphere model (cam 5.0)*. NCAR Tech. Note NCAR/TN-486+ STR.

Neale, R. B., Richter, J. H., & Jochum, M. (2008). The impact of convection on enso: From a delayed oscillator to a series of events. *Journal of Climate*, *21*(22), 5904–5924. https://doi.org/10.1175/2008jcli2244.1

Norris, J., Hall, A., Neelin, J. D., Thackeray, C. W., & Chen, D. (2021). Evaluation of the tail of the probability distribution of daily and sub-daily precipitation in CMIP6 models. *Journal of Climate*, 1–61. https://doi.org/10.1175/JCLI-D-20-0182.1

Oueslati, B., & Bellon, G. (2013). Convective entrainment and large-scale organization of tropical precipitation: Sensitivity of the cnrm-cm5 hierarchy of models. *Journal of Climate*, *26*(9), 2931–2946. https://doi.org/10.1175/jcli-d-12-00314.1

Park, S., Shin, J., Kim, S., Oh, E., & Kim, Y. (2019). Global climate simulated by the seoul national university atmosphere model version 0 with a unified convection scheme (SAM0-UNICON). *Journal of Climate*, *32*(10), 2917–2949. https://doi.org/10.1175/jcli-d-18-0796.1

Pendergrass, A. G., & Hartmann, D. L. (2014). Changes in the distribution of rain frequency and intensity in response to global warming. *Journal of Climate*, *27*(22), 8372–8383. https://doi.org/10.1175/jcli-d-14-00183.1

Peters, O., & Neelin, J. D. (2006). Critical phenomena in atmospheric precipitation. *Nature Physics*, *2*, 393. https://doi.org/10.1038/nphys314

Raymond, D. J. (2000). Thermodynamic control of tropical rainfall. *Quarterly Journal of the Royal Meteorological Society*, *126*(564), 889–898. https://doi.org/10.1002/qj.49712656406

Rushley, S., Kim, D., Bretherton, C., & Ahn, M.-S. (2018). Reexamining the nonlinear moisture-precipitation relationship over the tropical oceans. *Geophysical Research Letters*, *45*, 1133–1140. https://doi.org/10.1002/2017gl076296

Sahany, S., Neelin, J. D., Hales, K., & Neale, R. B. (2012). Temperature–moisture dependence of the deep convective transition as a constraint on entrainment in climate models. *Journal of the Atmospheric Sciences*, *69*(4), 1340–1358. https://doi.org/10.1175/jas-d-11-0164.1

Schiro, K. A., Ahmed, F., Giangrande, S. E., & Neelin, J. D. (2018). Goamazon2014/5 campaign points to deep-inflow approach to deep convection across scales. *Proceedings of the National Academy of Sciences*, *115*(18), 4577–4582. https://doi.org/10.1073/pnas.1719842115

Schiro, K. A., Neelin, J. D., Adams, D. K., & Lintner, B. R. (2016). Deep convection and column water vapor over tropical land versus tropical ocean: A comparison between the amazon and the tropical western pacific. *Journal of the Atmospheric Sciences*, *73*(10), 4043–4063. https://doi.org/10.1175/jas-d-16-0119.1

Seland, Ø., Bentsen, M., Olivié, D., Toniazzo, T., Gjermundsen, A., Graff, L. S., et al. (2020). Overview of the norwegian earth system model (NorESM2) and key climate response of cmip6 deck, historical, and scenario simulations. *Geoscientific Model Development*, *13*(12), 6165–6200. https://doi.org/10.5194/gmd-13-6165-2020

Semmler, T., Danilov, S., Gierz, P., Goessling, H. F., Hegewald, J., Hinrichs, C., et al. (2020). Simulations for CMIP6 with the AWI climate model AWI-CM-1-1. *Journal of Advances in Modeling Earth Systems*, *12*(9), e2019MS002009. https://doi.org/10.1029/2019ms002009

Swart, N. C., Cole, J. N., Kharin, V. V., Lazare, M., Scinocca, J. F., Gillett, N. P., et al. (2019). The Canadian earth system model version 5 (CanESM5. 0.3). *Geoscientific Model Development*, *12*(11), 4823–4873. https://doi.org/10.5194/gmd-12-4823-2019

Tatebe, H., Ogura, T., Nitta, T., Komuro, Y., Ogochi, K., Takemura, T., et al. (2019). Description and basic evaluation of simulated mean state, internal variability, and climate sensitivity in MIROC6. *Geoscientific Model Development*, *12*(7), 2727–2765. https://doi.org/10.5194/gmd-12-2727-2019

Tian, B., & Dong, X. (2020). The double-itcz bias in CMIP3, CMIP5, and CMIP6 models based on annual mean precipitation. *Geophysical Research Letters*, *47*, e2020GL087232. https://doi.org/10.1029/2020gl087232

Voldoire, A., Saint-Martin, D., Sénési, S., Decharme, B., Alias, A., Chevallier, M., et al. (2019). Evaluation of CMIP6 deck experiments with CNRM-CM6-1. *Journal of Advances in Modeling Earth Systems*, *11*(7), 2177–2213. https://doi.org/10.1029/2019ms001683

Wang, Y., Zhou, L., & Hamilton, K. (2007). Effect of convective entrainment/detrainment on the simulation of the tropical precipitation diurnal cycle. *Monthly Weather Review*, *135*(2), 567–585. https://doi.org/10.1175/mwr3308.1

Watanabe, M., Chikira, M., Imada, Y., & Kimoto, M. (2011). Convective control of enso simulated in miroc. *Journal of Climate*, *24*(2), 543–562. https://doi.org/10.1175/2010jcli3878.1

Wolding, B., Dias, J., Kiladis, G., Ahmed, F., Powell, S. W., Maloney, E., & Branson, M. (2020). Interactions between moisture and tropical convection. Part i: The coevolution of moisture and convection. *Journal of the Atmospheric Sciences*, *77*(5), 1783–1799. https://doi.org/10.1175/jas-d-19-0225.1

Wu, T., Lu, Y., Fang, Y., Xin, X., Li, L., Li, W., et al. (2019). The Beijing Climate Center climate system model (BCC-CSM): The main progress from CMIP5 to CMIP6. *Geoscientific Model Development*, *12*(4), 1573–1600. https://doi.org/10.5194/gmd-12-1573-2019

Xie, S., Wang, Y.-C., Lin, W., Ma, H.-Y., Tang, Q., Tang, S., & Zhang, M. (2019). Improved diurnal cycle of precipitation in E3SM with a revised convective triggering function. *Journal of Advances in Modeling Earth Systems*, *11*(7), 2290–2310. https://doi.org/10.1029/2019ms001702

Yukimoto, S., Kawai, H., Koshiro, T., Oshima, N., Yoshida, K., & Urakawa, S. (2019). The meteorological research institute earth system model version 2.0, MRI-ESM2.0: Description and basic evaluation of the physical component. *Journal of the Meteorological Society of Japan. Ser. II*. https://doi.org/10.2151/jmsj.2019-051

Zhang, G. J., & McFarlane, N. A. (1995). Sensitivity of climate simulations to the parameterization of cumulus convection in the Canadian climate centre general circulation model. *Atmosphere-Ocean*, *33*(3), 407–446. https://doi.org/10.1080/07055900.1995.9649539

Zhang, G. J., & Song, X. (2009). Interaction of deep and shallow convection is key to Madden-Julian Oscillation simulation. *Geophysical Research Letters*, *36*. https://doi.org/10.1029/2009gl037340

Ziehn, T., Chamberlain, M. A., Law, R. M., Lenton, A., Bodman, R. W., Dix, M., & Srbinovsky, J. (2020). The Australian Earth System Model: ACCESS-ESM1. 5. *Journal of Southern Hemisphere Earth Systems Science*, *70*(1), 193–214. https://doi.org/10.1071/es19035